Supporting Online Material for

A High-Frequency Secondary Event During the 2004 Parkfield Earthquake

Bettina P. Allmann,* Peter M. Shearer

*To whom correspondence should be addressed. E-mail: ballmann@ucsd.edu

Published 23 November 2007, *Science* **318**, 1279 (2007)
DOI: 10.1126/science.1146537

This PDF file includes:

Supporting online material

Methods

The full-waveform backprojection follows the method developed for the 2004 Sumatra-Andaman earthquake (*S1*) with some modifications warranted by the different source-receiver geometry for a local earthquake. First, our image volume is now 3D and does not require an *a priori* assumption of a fault plane. For display purposes, however, we calculate the result in two planes: one vertical plane that follows the known SAF fault trace, and one horizontal depth slice at the respective maximum backstacked amplitude. Second, the uneven station distribution and the finite aperture of the array required the use of a distance-dependent weight function (taper) during stacking, which is a well-known method to reduce migration artifacts (*S2*). In the presented images, we apply a linear taper for stations with radial distances between 10 km and 60 km from the respective image point.

We scale the amplitudes of our input velocity seismograms by means of an automatic gain control (AGC) algorithm in which we normalize the amplitudes within a running 10 s window to the maximum amplitude encountered in that window. This has the effect of equalizing the amplitude of the subevent relative to the mainshock, in order to balance the amplitudes in the backstacking result. The seismic amplitudes are usually strongest nearest the source and at early times. Consequently, to emphasize important signals at later times we scale the data as described. The final backstacked image amplitudes are squared to obtain a value proportional to energy.

Static time shifts to correct for variations in the near-surface are obtained by a two-step approach: first we calculate shifts using waveform cross-correlations to obtain the maximum coherency of the first arrival. Second, we force the aligned first arrivals to focus at the hypocenter by subtracting the forward-calculated traveltimes to the hypocenter from the onset of the

aligned waveforms. The static shifts vary between -0.4 s and 1.0 s. Using the shallowest velocity in our model of 1.3 km/s, these statics are likely generated in the topmost 0.5 km to 1.0 km of the crust.

To directly locate the secondary phase seen on individual seismograms, we apply a grid-search along the assumed fault plane and in the respective depth slice to minimize the difference between predicted t_i^p and observed traveltimes t_i . To estimate the misfit χ^2 between predicted t_i^p and observed t_i traveltimes of the least-squares inversion, we define

$$\chi^2 = \sum_{i=1}^{n} \frac{[t_i - t_i^p]^2}{\sigma^2} \tag{1}$$

where n is the number of stations and σ is the standard deviation of the residuals at the best-fitting location. The expected value of χ^2 is the number of degrees of freedom ndf. In our study ndf equals 17. To compute the theoretical traveltime we use different 1-D velocity models for the local Parkfield stations and the regional southern California stations, respectively.

Synthetic backprojection test

We carried out a synthetic test in order to determine the spatial resolution kernel of our given source-receiver geometry. Synthetic seismograms at all 73 local strong-motion stations are generated using two point sources that are located 15 km apart at a depth of 7.9 km and occur 5 s apart. Each point source consists of a 5 Hz Ricker wavelet. The backprojection method was applied to the synthetic data, and the resulting stack over all times between 2 s before and 10 s after the alignment is shown in *Fig. S1*. The two sources are well recovered. The resolution kernel for each source is elliptical with a 90° rotation angle in the direction of the major axis between the two sources. We applied the same linear station distance weighting as in the real data in order to reduce artifacts. For an ideal station distribution, the spatial resolution at the hypocenter is limited to the wavelength within the investigated frequency band, which is about

1 km (at 4 Hz). In addition, inaccuracies in the velocity model and statics can lead to defocusing of the subevent with respect to the hypocenter.

Backprojection time slices

The backprojected images for all consecutive 0.5 s time slices between 2 s before and 10 s after the alignment show a clear focus at the hypocenter location between 0.5 s to 1.5 s, which is not surprising since we force the image to focus at this point using the static correction computed using waveform cross-correlation (*Fig. S2*). We observe a second clear focus north of the hypocenter about 5 s later. Circularly shaped artifacts from backprojection of the initial part of the S wave are of similar amplitudes as the signal from later parts of the seismograms, which makes it difficult to distinguish between them. If we mute the first 2 s of the S wave from each seismogram in order to concentrate on the later signal, the second focus point north of the hypocenter between 5.5 s and 6.5 s becomes more prominent and some of the circular high amplitude artifacts can be reduced (*Fig. S3*). This test is to check whether the subevent could be an artifact caused by the enforced coherence at the hypocenter. These are the images presented in *Fig. 1B* in the manuscript.

Time history of backprojection

In order to study the time history of the rupture propagation along the fault, we stack the back-projected fault image for all time slices (a 3D volume in strike, depth, and time) over a depth interval and display the result as distance along strike versus time (*Fig. S4*). This also allows us to directly estimate the rupture velocity. The two point sources from the synthetic data are well recovered (*Fig. S4A*). The first source focuses at zero time and the second source 5 s later, 15 km to the north of the hypocenter, which results in a rupture velocity of 3 km/s. However, linear artifacts are present that make a precise estimate difficult. The real data result shows two

clear focus points, one at zero time at the mainshock hypocenter and a second focus about 5 s later, 12.5 km to the north (*Fig. S4B*). From this we estimate an average rupture velocity of about 2.5 km/s. This result also shows that either there was no continuous rupture propagation between the hypocenter and the subevent, or that the radiated seismic energy in this area is much less than that from the two main areas of radiation. We have therefore no evidence for a change in rupture velocity.

Comparison to other results

The largest coherent high-frequency event observed in the UPSAR array by (*S3*) is consistent with a source location at our subevent, even though (*S3*) reported a location about 4 km south of our secondary event and about 5 km deeper (*Fig. 4C*). If only the UPSAR data are used for location estimates, the source location error is considerable, due to the narrow aperture of the UPSAR array: if we map the difference between traveltimes from UPSAR stations to the best-fitting location and traveltimes from UPSAR stations to any other point on the fault plane, we notice that the ellipse defined by a traveltime difference of half a wave period will encompass the best-fitting location derived in this paper. The location error of our result is considerably smaller due to the more favorable geometry with stations being evenly distributed around the location of the subevent.

Seismic moment and scaled energy estimation

The scaled energy (*S4*) is defined as $\tilde{e} = E_R/M_0$, where E_R is the radiated seismic energy and M_0 the scalar seismic moment. It is a useful dynamic parameter for comparing the characteristics of earthquakes.

The scalar seismic moment is given by $M_0 = \mu \bar{D} A$, where μ is the shear modulus, $\bar{D}$ the average displacement (slip), and A the slip area. We can estimate the ratio of M_0 between

the area around the mainshock hypocenter and the subevent from the different slip inversion models. The result for different models is highly variable and we estimate that the northern slip patch had 2 to 20 times higher moment release than the slip near the hypocenter.

Uncertainties in estimates of E_R are large, because this requires accurate accounting for the effects of site amplification, attenuation, scattering, and other effects. We minimize the above uncertainties by comparing only the relative energy released from the hypocenter and the subevent location. We estimate the ratio of radiation, E_{HF}, from the sum over the squared amplitude from unfiltered velocity seismograms over two 1.2 s time windows around the theoretical S-arrival from the hypocenter and the subevent location at each of the local strong-motion stations used for backprojection. The sum is computed over both horizontal components. Since we estimate the ratio of radiated seismic energy between mainshock and subevent from the same seismograms, we do not have to correct for local station-specific site effects. The ratios obtained from each individual station are averaged for all stations in an attempt to remove directivity effects. We also apply a simple geometrical spreading correction by multiplying the sums with the squared distance between the station and the mainshock hypocenter, or the subevent location, respectively. The resulting ratios suggest comparable or greater energy radiation from the mainshock hypocenter, although the scatter is very high. The median ratio over all stations suggests about five times more energy radiation from the hypocenter. The UPSAR stations seem to be an exception with higher E_{HF} estimates from the subevent area. A further complication is that the secondary arrival has higher amplitude in the P_n arrivals observed in the data of regional stations greater than 100 km to the south (see *Fig. 3*). However, the P_n records are at lower frequencies and it is also possible that these P_n amplitudes are biased because we selected only those records with the clearest (and highest amplitude) secondary arrivals. Taken together, the higher M_0 and the lower E_{HF} release for the subevent area suggest a lower $\tilde{e}$ for the northern slip patch compared to the hypocenter, assuming that the total radiated seismic energy, E_R, is

proportional to that measured in the strong motion seismograms. Stress drop is likely spatially varying over the fault surface and our argument here for a relatively low stress drop for the northern slip event applies to the average stress drop over the entire slip patch. It is likely that the HF subevent itself involved a higher stress drop within a more localized part of the fault.

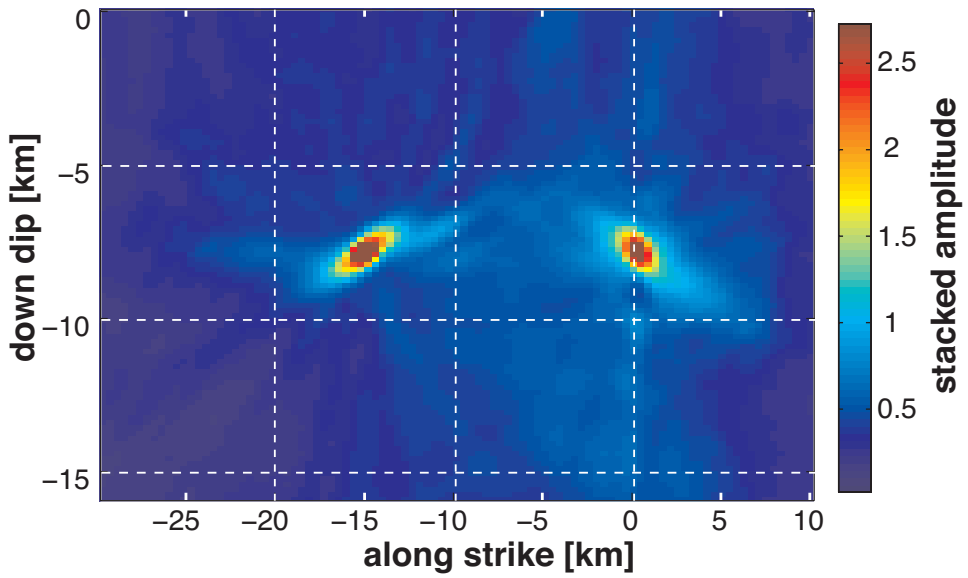

Figure S1: Cumulative radiated energy over 12 s from 2 s before to 10 s after the aligned traces for synthetic seismograms with two point sources 15 km apart. A linear station distance weighting is applied to the data. Both point sources are well recovered.

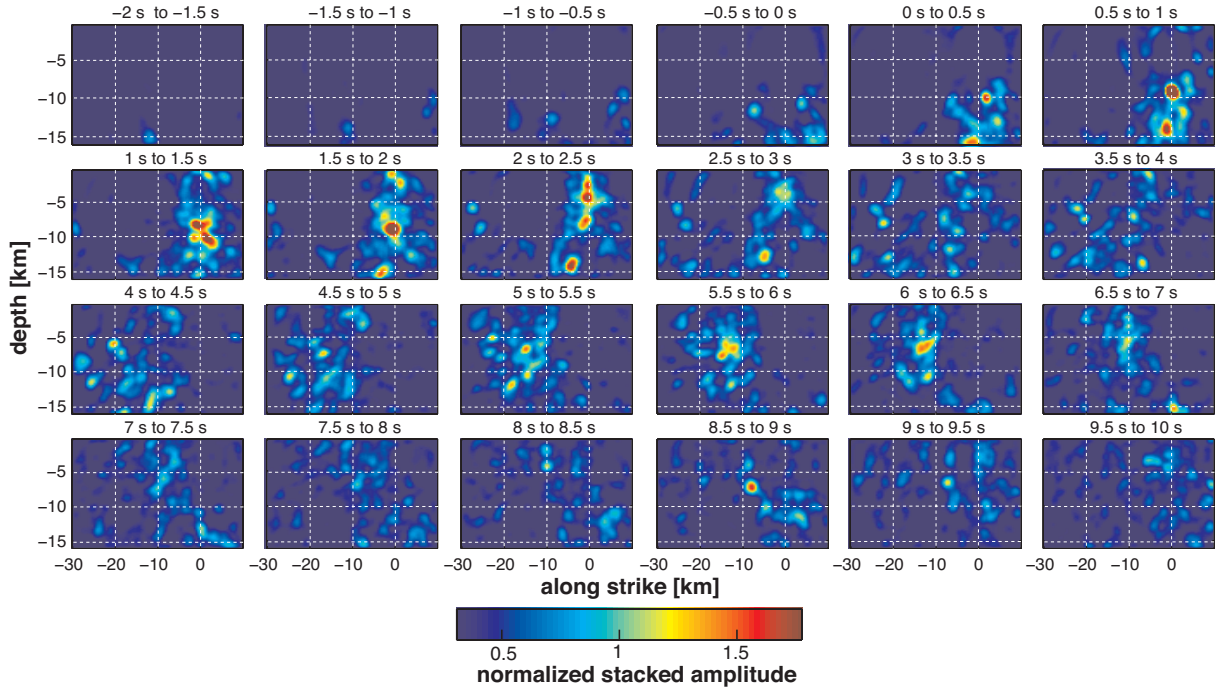

Figure S2: Consecutive 0.5 s time slices of backprojected radiated energy. A linear station distance weighting is applied to the data.

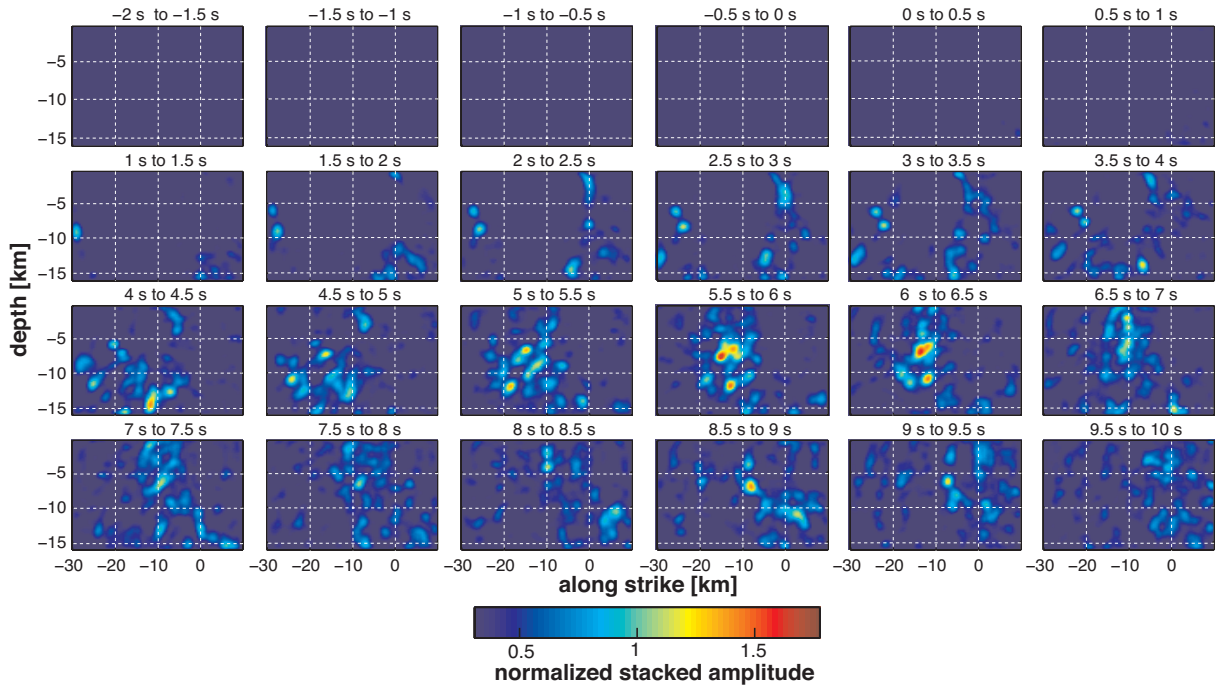

Figure S3: Consecutive 0.5 s time slices of backprojected radiated energy. A linear station distance weighting is applied to the data. The first two seconds of each seismogram after the alignment are muted in order to concentrate on the later signal.

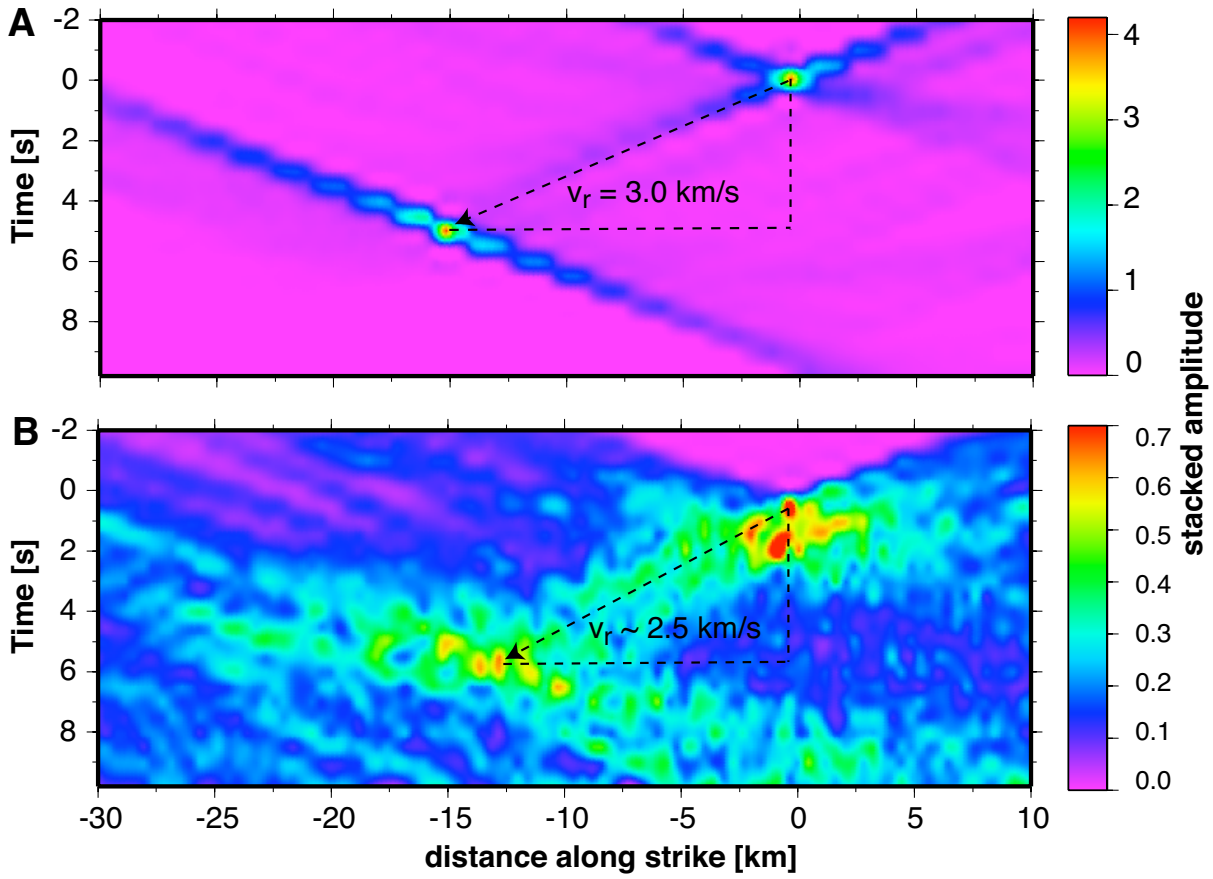

Figure S4: Time-distance plot of a stack over a depth interval of 2 km to 12 km of radiated seismic energy. **A)** Synthetic results for two point sources (see *Fig. S1*). **B)** Real data results. The estimated average rupture velocity between the mainshock hypocenter and the subevent is 2.5 km/s.

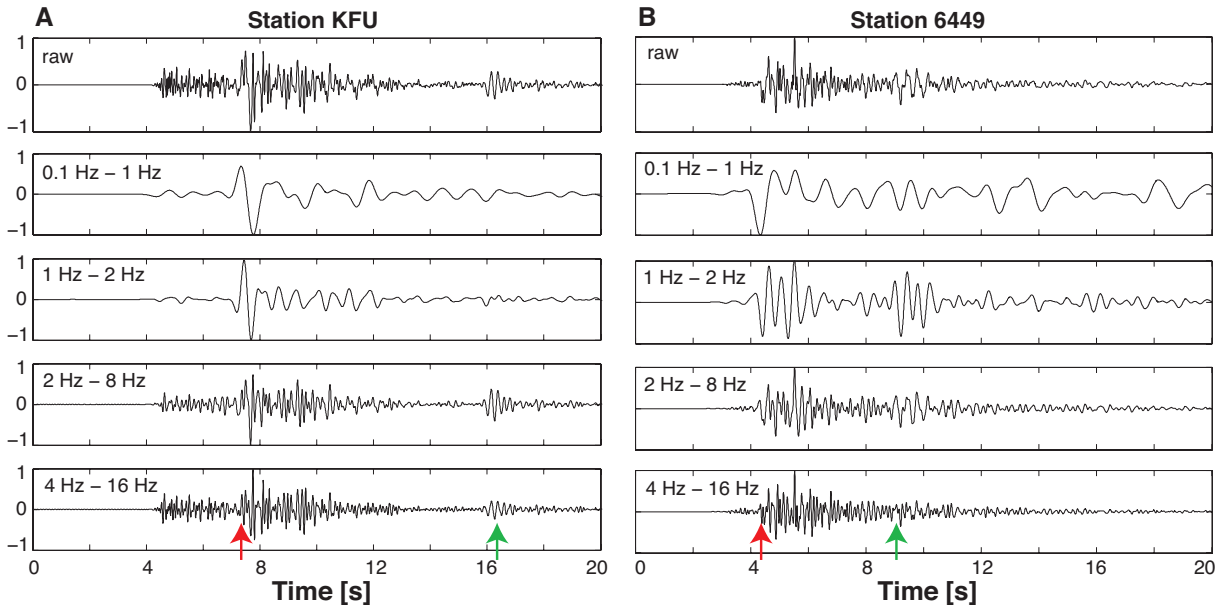

Figure S5: Different bandpass filters applied to seismograms from two stations that show clear secondary S-wave arrivals. **A)** Station KFU. **B)** Station 6449. From top to bottom: raw trace, 0.1 to 1 Hz, 1 to 2 Hz, 2 to 8 Hz, and 4 to 16 Hz. Note that the secondary event is better seen at higher frequencies above 1-2 Hz . The red and green arrows mark the S arrival of the mainshock and subevent, respectively.

References and Notes

S1. M. Ishii, P. M. Shearer, H. Houston, J. E. Vidale, *Nature* **435** (2005).

S2. T. Hertweck, C. Jaeger, A. Goertz, J. Schleicher, *Geophysics* **68**, 1673 (2003).

S3. J. Fletcher, P. Spudich, L. Baker, *Bull. Seismol. Soc. Am.* **96**, 129 (2006).

S4. H. Kanamori, L. Rivera, *Geophysical Monograph Series* **170**, 3 (2006).